Brell, M., Rogaß, C., Segl, K., Bookhagen, B., Guanter, L. (2016): Improving Sensor Fusion: A Parametric Method for the Geometric Coalignment of Airborne Hyperspectral and Lidar Data. - *IEEE Transactions on Geoscience and Remote Sensing*, *54*, 6, pp. 3460–3474.

DOI: http://doi.org/10.1109/TGRS.2016.2518930

Improving sensor fusion: A parametric method for the geometric co-alignment of airborne hyperspectral and lidar data

Maximilian Brell[1,*], Christian Rogass[1], Karl Segl[1], Bodo Bookhagen[2], Luis Guanter[1]

1. Helmholtz Centre Potsdam–GFZ German Research Centre for Geosciences, Section 1.4 Remote Sensing, Telegrafenberg, 14473 Potsdam, Germany
2. University of Potsdam, Institute of Earth and Environmental Science, Karl-Liebknecht-Str. 24-25, 14476 Potsdam-Golm, Germany

* Corresponding author; E-Mail: brell@gfz-potsdam.de;
Tel.: +49-331-288-1195; Fax: +49-331-288-1192.

Abstract

Synergistic applications based on integrated hyperspectral and lidar data are receiving a growing interest from the remote-sensing community. Pre-requisite for the optimum sensor fusion of hyperspectral and lidar data is an accurate geometric co-alignment. The simple unadjusted integration of lidar elevation and hyperspectral reflectance causes a substantial loss of information and does not exploit the full potential of both sensors. This paper presents a novel approach for the geometric co-alignment of hyperspectral and lidar airborne data based on their respective adopted return intensity information. The complete approach incorporates ray tracing and subpixel procedures in order to overcome grid inherent discretization. It aims at the correction of extrinsic as well as intrinsic (camera resectioning) parameters of the

hyperspectral sensor. In additional to a tie point based co-registration, we introduce a ray tracing based back projection of the lidar intensities for area-based cost aggregation is introduced. The approach consists of three processing steps: First, a coarse automatic tie point based boresight alignment. The second step co-registers the hyperspectral data to the lidar intensities. Third, a parametric co-alignment refinement with an area-based cost aggregation. This hybrid approach of combining tie point features as well area-based cost aggregation methods for the parametric co-registration of hyperspectral intensity values to their corresponding lidar intensities results in a root mean square error of 1/3 pixel. It indicates that a highly integrated and stringent combination of different co-alignment methods leads to an improvement of the multi sensor co-registration.

Keywords: imaging spectroscopy; airborne laser scanning (ALS); direct georeferencing; parametric georeferencing; rigorous geocoding, co-registration; sensor fusion; multi-sensor; pre-processing; ray tracing; sensor alignment

1 Introduction

Data fusion is a common method for the improvement of data quality and information content in remote-sensing measurements. A challenging example is the fusion of airborne hyperspectral and lidar data, which allows to integrate high spectral resolution with high-resolution spatial information. The fusion of both data types with the purpose of completing or enhancing a comprehensive object characterization is important and promising, especially for heterogeneous environments [1] and steep terrain. Different studies have already proven the potential of integrating lidar and hyperspectral imaging (HSI) data for various areas of research, including urban [2] [3], forest [4] [5] [6] [7] [8] and ecological applications [9] [5] [10]. For data analysis

and classification procedures, the elevation information serves as an additional dimension to enhance information content and classification results.

An overall prerequisite and therefore one of the most important steps for proper data fusion is the accurate geometric co-registration or co-alignment of both sensor entities. For example, a misalignment between lidar and HSI sensors of ± 3 pixel root mean square (RMS) in both X and Y directions leads to a significant reduction of data information content, depending on the heterogeneity of the mapped targets [1]. Therefore, a proper geometric co-alignment of both sensors is indispensable for accessing the entire information content of both data entities. Additionally, a perfect co-alignment is also a precondition for a radiometric, spectral and spatial fusion of HSI and lidar sensors. Standard direct geometrical pre-processing of HSI data under practical, non-optimized conditions result in absolute geometric accuracy of 1 – 3 pixel [11]. Therefore, HSI systems often do not meet the spatial requirements of applications concerning accuracy and resolution. This is caused by variable, intrinsic optical aberrations in the sensor design and the lack of standardized data pre-processing workflows. In comparison to that, the geometric accuracy of modern lidar systems is significantly higher. They can reach vertical accuracies of smaller 20 cm [12] and horizontal accuracies of a few decimetre depending on the flight parameters, pre-processing, terrain slope and the reflectivity of the targets. Often, the lidar data is taken as a geometric reference for the spatial fusion with HSI data.

Standard fusion of HSI and lidar is limited by the integration of the separated data entities, the gridded hyperspectral data cube (X, Y, Spectrum) and the gridded Digital Elevation Model (X, Y, Z). Usually, both data entities are generated in separated pre-processing workflows. The gridded elevation model is only considered during the direct geocoding [13] [11] and atmospheric correction [14] of the HSI data. A proper

geometric co-alignment is assumed but not explicitly performed. In contrast, advanced fusion approaches include a geometrical co-alignment procedure as a central pre-processing step. There exist many variations, because the broad term fusion for lidar and HSI data is indefinite and does not implicate a standardized method or level of implementation. In general, existing fusion approaches share the aim of enhancing the information content but differ by the chosen level of implementation and method. Physical or empirical fusion methods are applied to different data or product levels [15]. For the geometric co-alignment of lidar and hyperspectral data, various methods exist and they can be distinguished into parametric (physical) and non-parametric (empirical) approaches. Non-parametric approaches attempt to compensate the geometric errors by adjusting the pre-processed gridded data sets during post-processing. They employ area-based- or feature-based detection algorithms in both data entities and perform an interpolation or resampling-based rectification to a common image plane [16] [3]. In general, non-parametric approaches require sufficient, homogenous distributed and detectable objects or intensity gradients in both scenes. Especially for low-contrast and homogeneous scenes these requirements are not fulfilled and result in rubber-sheeting problems between the detected objects. Therefore, area-based non-parametric intensity methods [17] are very sensitive to illumination and spatial response differences, which are inherent in lidar and HSI images. In contrast, parametric approaches try to minimize the systematic error budget during the data pre-processing procedure. They need background information for sensor parameters, positioning and attitude in addition to the raw sensor data [1]. Parametric co-alignment strategies attempt to assign generally valid offset parameters (see Table II: Overview of parameters optimized in the co-alignment approach) to the global parametric geocoding procedure [8]. These offset parameters are determined by minimizing the

distances between local features, which are detectable in a small subset of both overlapping sensor datasets. Therefore, parametric methods are less influenced by their respective radiometric response of the sensors and an additional extensive radiometric adaptation is not imperative. Hence, they are well suited for the fusion of active and passive sensors enabling a separate geometric and radiometric fusion. However, since parametric approaches are tie-point based and usually carrier out on a pixel level, they do not completely describe the geometric fit of more complex features. Altogether, the gridded integration or comparison of both data entities is limited and not ideal for high geometric accuracies, because it results in spectral and spatial discretization and, therefore, in a substantial information loss [18].

The aim of this paper is to develop a co-alignment method avoiding the known drawbacks of parametric and non-parametric methods which can simultaneously handle the inherent geometric drawbacks of hyperspectral sensors and different sensor responses without rasterized discretization. This results in a novel approach for the improved geometric fusion of hyperspectral imaging sensors and lidar sensors starting at a sensor-driven data level. The key element is the definition and implementation of a robust parametric co-alignment procedure to minimize the inherent error budget of the HSI sensor in relation to the lidar intensity data. Our developed hybrid approach integrates an area-based cost aggregation often used in non-parametric approaches into a parametric approach often limited to feature-based alignment. It is based on the main software modules of the in-house software “HyPrepAir” which are developed for hyperspectral airborne pre-processing.

2 General HSI and lidar sensor system characteristics

Both sensor systems differ fundamentally in their function and data collecting principles. HSI systems are passive sensors collecting electromagnetic solar

irradiation reflected from the earth surface towards the sensor. HSI systems can measure reflected radiance in the visual to near infrared (400 – 1000 nm VNIR) and short wave infrared domain (1000 – 2500 nm SWIR). The high spectral resolution of the HSI sensor results in an almost continuous spectrum [19] [20]. In contrast, lidar systems are active sensors emitting pulsed radiation of one narrow bandwidth towards the earth surface (Fig. 1 left). Lidar systems usually emit and receive very narrow monochromatic wavelength ranges of 532 nm, 1064 nm or 1550 nm. The reflected radiation intensity as well as the time-of-flight (TOF) of the laser pulse is measured. A 3D point cloud (X, Y, Z) with the intensities values of the reflected laser pulses is the result. Both sensors potentially operate in the visible and infrared wavelength domain and share an overlapping wavelength range (Fig. 1 right). This overlapping wavelength range is the main linkage between both sensor systems and the basic requirement of the developed parametric-based co-registration.

The bandwidth of the lidar impuls is very short in comparison to bandwidths of the HSI (5-20 nm full width at half maximum (FWHM)). A Gaussian spectral response function (SRF) with the intensity maximum in the centre of the function can be assumed for every band of both sensors [20].

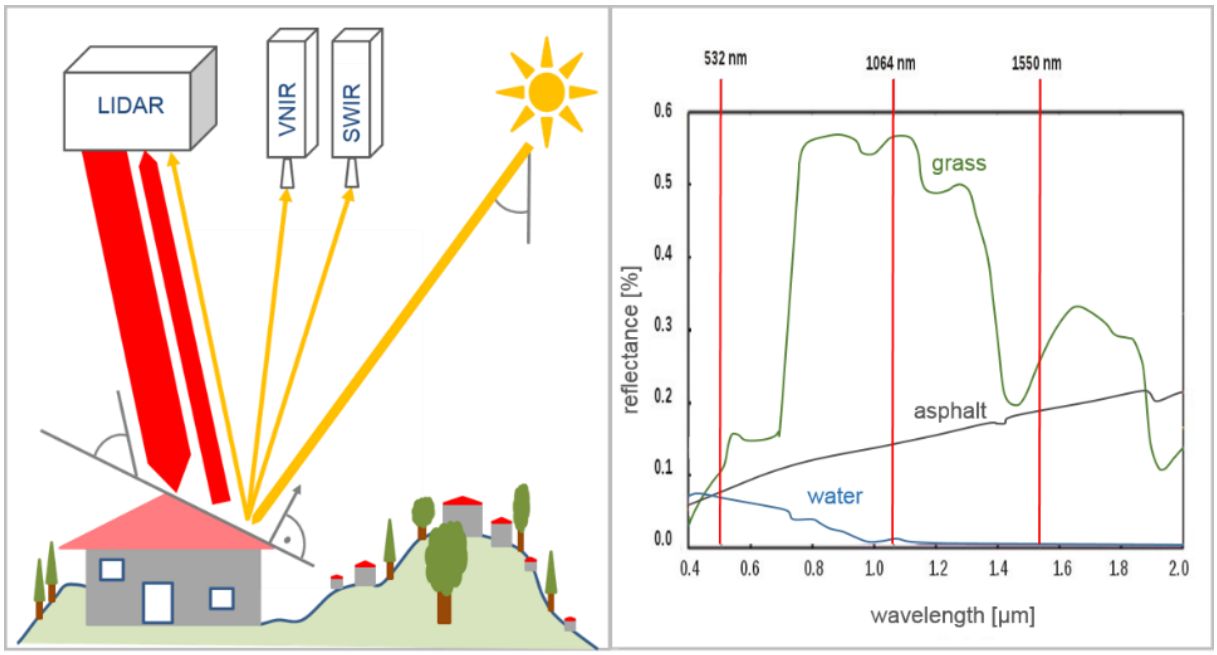

Fig. 1: Different radiation models for the sensors (left), possible wavelength overlaps between lidar and HSI systems (right). Red vertical lines show common laser wavelengths drawn over characteristic spectra for grass (green), asphalt (black), and water (blue).

Modern HSI systems are usually designed as pushbroom scanners because of longer integration times that improve their signal-to-noise ratio (SNR) of the data. The recorded reflected radiation per scanline is dispersed by a grating or prism into spectral fractions and thereby projected to discrete rows of the full frame sensor array [19]. The geocoding procedure follows the collinearity relations [13] [11]. Based on the attitude and position of the airplane measured by the global position system (GPS) and the Inertial Measurement Unit (IMU) at a given point in time, each image pixel can be geocoded with its pointing characteristics. These characteristics are also affected by non-uniformities in the spatio-spectral frames of the pushbroom imaging spectrometer called keystone [21] [22] and smile [21] effects.

The lidar sensor is a whiskbroom system. A rotating mirror is deflecting the emitted laser pulses in varying angels and high repetition rates (up to 400 kHz) in the direction of the earth surface. A receiver measures the reflected intensity and its chronological sequence (full waveform) [23] [24]. The direction and duration of every

laser impulse in combination with the attitude and position of the sensor enables the calculation of the location and distance of the reflecting surface.

2.1 Spatial sampling characteristics

Due to the different sensor designs, the spatial data acquisition results in different sampling distributions and sampling densities. Lidar systems have a wide field of view (FOV; < 60°). During one mirror rotation up to 400,000 pulses with a short delay in time are emitted. The movement of the airplane causes a shift of every lidar point. The sampling density decreases with off-nadir direction, which is compensated by overlapping flight stripes. The laser beam has a small divergence of less than 0.5 mrad, which results in altitude dependent footprint diameters [23] [24]. The generated point density and ground sampling distance (GSD) is dependent on the flight speed above ground and altitude of the airplane.

HSI sensors usually have a smaller FOV and therefore a narrow swath. The GSD between every pixel centre in a sensor row is defined by the instantaneous field of views (IFOV) in across and along track direction, the time frame between two scanlines, flight speed and attitude [20]. The IFOVs and the pointing of the sensor elements are not regular due to the sensor design and sensor motion. This results in an irregular pointing in across and along track direction [20]. The high spectral resolution of the HSI sensor is at an expense of the spatial resolution and accuracy. VNIR and SWIR sensors are often designed as separated sensors. SWIR sensors have a lower spectral and sometimes spatial resolution than VNIR sensors, because of the significantly reduced radiance in the SWIR wavelength range. The sampling distribution of the pushbroom sensor is more regular compared to the whiskbroom lidar sensor, because one entire scanline is measured simultaneously [20]. In summary, the initial spatial sampling distribution patterns generated by airborne lidar

and HSI sensors are completely different and irregular and have to be resampled onto regular grids for further processing.

2.2 Challenge of the geometric co-registration

Sensor model, position and attitude accuracy (IMU/GPS) as well as alignment errors (lever arm, boresight and synchronization) are the main error sources influencing the geometric alignment. Fig. 3 shows the scheme of the system integration and the inherent alignment errors. The boresight offset (offsets angle introduced by the dislocation of the image projection centre and the IMU origin of coordinate) as well as the lever arm (dislocation between the GPS antenna and the IMU origin of coordinate) have to be corrected for every sensor separately. All sensors are dependent on the delivered IMU/GPS accuracy which also introduces geometric errors to the lidar and HSI data. Due to their complicated sensor design and their passive character described above, HSI sensors have certain drawbacks (strong central perspective, keystone, lower spatial resolution) in comparison with geometrically highly specialized lidar sensors. Additionally, HSI sensors are usually geometrically and spectrally calibrated under laboratory conditions [25] [26] [27]. However, under practical flight conditions pressure and temperature changes, as well as vibration and accelerations influence the sensor geometry to a certain degree. Because of the large distances between target and sensor, even small distortions lead to conspicuous spatial aberrations that affect the co-alignment of the sensors.

The physical linkage between spatial and spectral domains of both sensor responses has to be considered for sensor fusion [28]. The adaptation of the different spatial and spectral responses of the sensors is the main challenge. These response differences are clearly recognizable by comparing the intensity images in the overlapping wavelength of the lidar sensor (Fig. 4 left) with the intensity images of the

SWIR sensor (Fig. 4 right). A radiometric calibration of the lidar intensities itself is not performed yet, because the differences of the intensities are dominated by the passive character of the HSI intensities. Hence, the developed geometric co-alignment procedure should be robust enough to operate independent of a cross-calibration. Altogether, the complete co-alignment should avoid unnecessary resampling procedures to conserve the original data quality. In addition, the large data amount is an additional challenge that has to be handled efficiently to enable pre-processing of large flight campaigns.

3 Method

The developed method for in-flight geometrical alignment of airborne hyperspectral and lidar intensity data can be separated into three principle parts (Fig. 2):

- Input data generation and pre-processing of the input data
- Geometric alignment workflow
- Geometric correction

It includes the in-flight airborne sensor integration and data acquisition strategy as well as the geometric co-alignment approach itself. After data acquisition and pre-processing of the lidar and HSI data a spectral and spatial response adaptation (Fig. 2 rhomb 4 & 5) is realized. The parametric co-registration itself is a three-step alignment procedure (Fig. 2 rhomb 6) based on optimizing extrinsic as well as intrinsic alignment parameters. In a first step, a coarse tie-point based co-alignment of overlapping HSI stripes is realized. The second step co-aligns the HSI image to the lidar intensity image with the use of tie points. The third step is an intensity and area-based cost aggregation. This method compares the template HSI intensities of three sensor rows with the corresponding lidar intensities calculated for different offsets parameter. The corresponding lidar intensities are generated by a ray tracing based

geometric intersection of the HSI sensor element pointing, represented by a cone, with the lidar point cloud. The geometric correction is the final procedure which assigns the determined offset parameters to the complete flight campaign. In the following, the three principle parts and their respective processing procedures are described in detail.

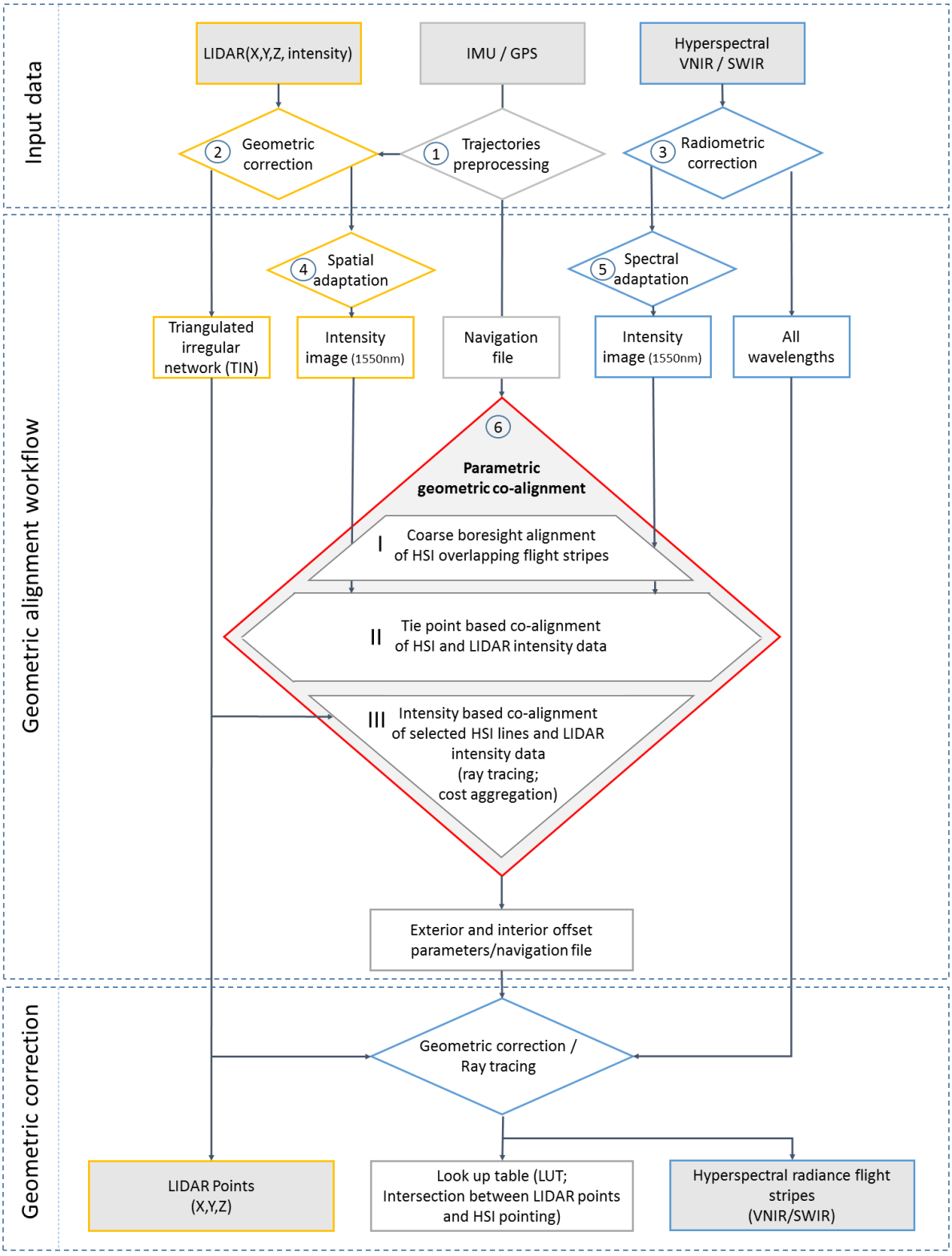

Fig. 2: Overview of the simplified geometric fusion workflow (rectangles represent data products; rhombs represent processing procedures; the lidar part is outlined in yellow; central linkage based on IMU/GPS data outlined in grey; the HSI part is outlined in blue; the central fusion step is outlined in red). The trajectories are the key linkage in the fusion workflow and therefore their pre-processing is the first step.

3.1 Input data generation

For input data generation the airborne sensor integration and data acquisition strategy has to be adopted to ensure a proper data quality. Additionally, the pre-processing part of the workflow (Fig. 2 rhomb's 1, 2 & 3) homogenizes the sensor outputs of the three different sensors to a data level, which can be used as a starting point for the determination of the global extrinsic and intrinsic alignment parameters (Table II).

3.1.1 Airborne sensor integration and data acquisition

For the development and testing of a geometric fusion algorithm a calibration flight campaign was realized. A Hyspex VNIR-1600 [29] and a Hyspex SWIR 320m-e [29] HSI sensor in combination with a lidar LMS-Q560 [30] were integrated inside a Cessna 207 Skywagon.

Table I gives an overview of the particular sensor parameters. An AEROcontrol-IId inertial measurement unit (IMU) with available data rates of 256 Hz in combination with a Novatel OEM4 - g2 GPS receiver was used for measuring the position and attitude of the airplane. The provided accuracy of position and attitude by the IMU/GPS is essential for the direct georeferencing of the sensors. The IMU is able to deliver post-processing accuracies of 0.004° RMS for roll and pitch and 0.01° RMS for heading.

Table I: Overview of used sensors and particular parameters

	Lidar (LMS-Q560)	VNIR and SWIR HSI (Hyspex)
Principle	active	passive
Sensor design	Whiskbroom (polygon mirror)	Pushbroom
FOV (Field of View)	60°	VNIR: 35.5° SWIR: 27.2°
IFOV (instantaneous field of view)	-	VNIR: across track 0.18 mrad along track 0.36 mrad

		SWIR: across track 0.75 mrad along track 0.75 mrad
Laser beam divergence	< 0.3 mrad	
Spectral range	1550 nm	VNIR: 400 - 1000 nm SWIR: 1000 – 2500 nm
Frames per second (HSI) Pulse frequency (lidar)	240 kHz (160 lines/s)	VNIR: 135 fps SWIR: 100 fps
Spectral sampling	monochromatic	VNIR: 3.7 nm SWIR: 6 nm
Pulse length	< 4ns	
FWHM (spectral)		VNIR: 1.0-2 pixel SWIR: 1.5-2 pixel
Spectral bands	1; Full Waveform	VNIR: 160 SWIR: 256
Spatial pixels hyperspectral		VNIR: 1600 SWIR: 320

Measurement setup, sensor operation and flight planning were adapted with the objective of generating an ideal data basis for a proper sensor fusion. The HSI (VNIR, SWIR), lidar and DGPS/IMU sensors were arranged on a passive damped aluminium plate. Their origins of ordinates were installed as close together as possible (Fig. 3). A static connection is established between the three sensors to avoid vibrations and spatial distortions between the sensors.

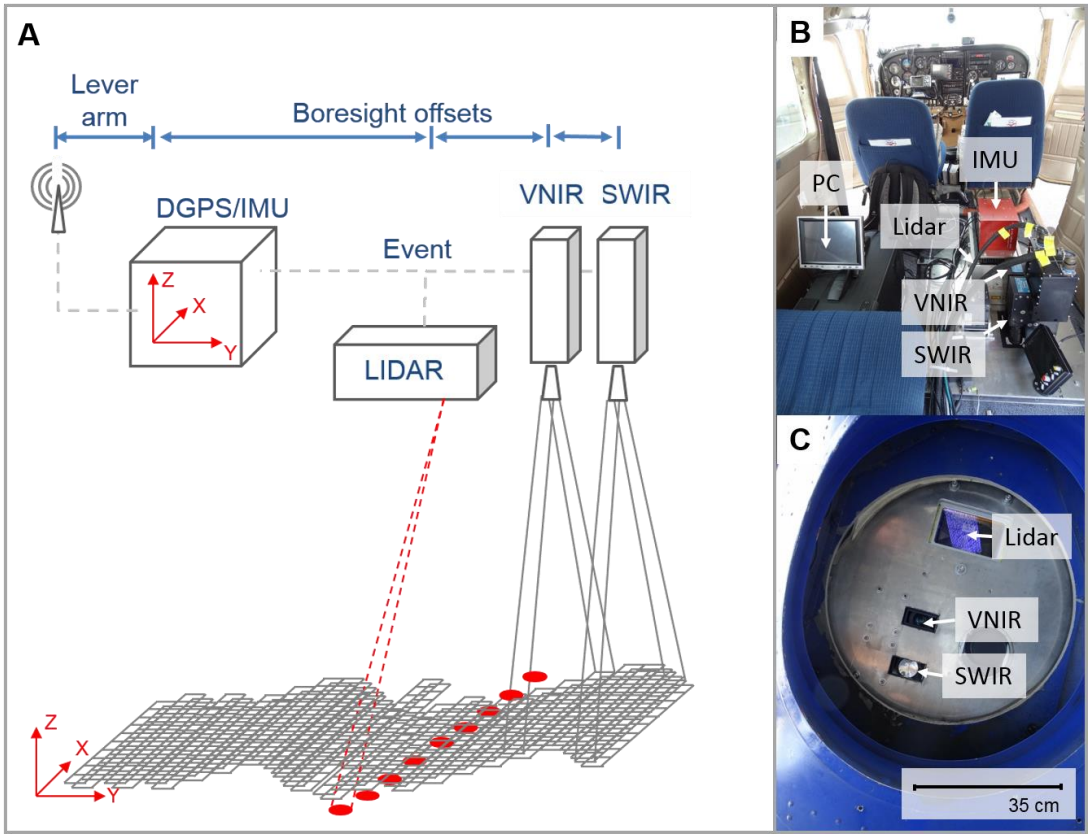

Fig. 3: (A) Scheme of airborne sensor integration and function principle (DGPS: Differential GPS, IMU: initial measurement unit). (B) Photo of sensor integration into the airplane and (C) photo of sensor integration below the airplane (C)

The test flight generated about 16 GB of HSI image data and about 1 GB of lidar point data (21 x10^6 points). The dataset consists of four flight lines (Fig. 4) flown 800 m above ground over an airfield bordering sub-urban development in Kamenz (Germany, 51.29063°N 14.12107°E). The terrain is relatively flat with a height range of 33 m. The heterogeneous sub-urban objects (buildings, roads, trees, fields) introduce most of the elevation changes, generating slopes up to 90° between surface objects. The flight altitude and the flight speed of about 190 km/h above ground result in a ground sampling resolution of about 1.5 m for SWIR and 0.8 m for VNIR. The lidar scanner generates a point density of about 5 points/m² in non-overlapping areas (100 lines per second, 150 kHz and 60° FOV parameterization).

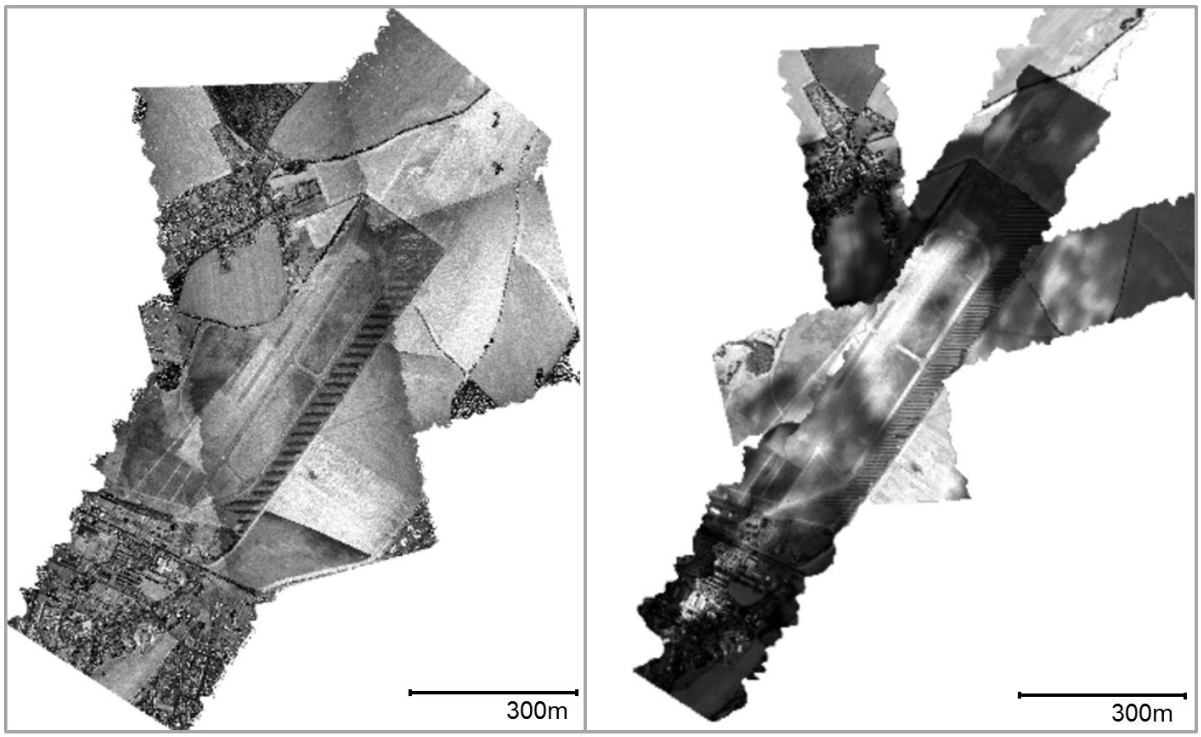

Fig. 4: Geocoded overview of the four flight lines; lidar intensity image 1550 nm (left), HSI SWIR intensity image 1550 nm (right)

3.1.2 Pre-processing of HSI, lidar and DGPS/IMU data

The pre-processing part of the data generated by the three sensors ensures the homogenization and provision of the required input data quality.

The parametric geocoding of the lidar and the HSI are based on the trajectories of the airplane that define the orientation and line of sight of the sensors. The trajectories are generated by combining the binary information of the position (GPS) and attitude (IMU). The differential post-processing (Fig. 2 rhomb 1) of the Differential Global Positioning System (DGPS) signal is realized by using phase and Doppler measurements of a nearby ground reference station with the software GrafNav^{TM}. The offset between GPS antenna and IMU origin of ordinates (lever arm) is corrected. High accuracy is guaranteed by integrating the DGPS with the IMU information. Both error dynamics are uncorrelated. Forward and reverse Kalman filtering is done in the post-processing procedure to minimize both errors. The

trajectory pre-processing was done with the software AeroOffice™. The trajectory optimization results in smooth best-estimation trajectories for the IMU/GPS origin of ordinate with state of the art accuracy for position (X0, Y0, Z0) and attitude (roll, pitch and heading). The output ASCII file provides the base of the direct geocoding of both sensors.

The geometric alignment workflow of the two sensors is based on an iterative co-registration of the HSI data to the lidar intensity data. Therefore, the geometric pre-processing of the lidar data (Fig. 2 rhomb 2) has to create accuracies that are high enough to serve as a geometric reference. This is achieved by a state-of-the-art geometric correction workflow including boresight alignment, single-flight stripe correction and relative flight stripe adjustment implemented in the software RiPROCESS™. Their overall strategy is to minimize the lidar inherent random and systematic error budget (instrument errors, trajectory errors, synchronization errors, atmospheric conditions).The resulting lidar point cloud is filtered with the software Terrasolid™. Erroneous lidar point outliers inside the point cloud are removed by analysing the height and spatial-neighbourhood relationships. This robust outlier removal enables an optimized geometric representation of the surface features. The resulting corrected 3D point cloud ensures very high positional accuracies. The backscattered lidar intensity information of the 3D points are subsequently used (3.2.1.2) for generating a gridded true orthoimage. The 3D point cloud itself is used as morphometric surface and elevation information. This point cloud is divided into regular spatial tiles, stored as separated files in the LAS format.

In a first step of the hyperspectral pre-processing, a radiometric correction (Fig. 2 rhomb 3) is applied to transform digital numbers (DN) into at-sensor-radiance values. The radiometric correction is accomplished by applying a linear transformation with

determined calibration coefficients (offset and gain) to every image pixel. The offset (that includes the thermally induced dark current) is determined automatically, by closing a shutter before (VNIR) or after (SWIR) every flight line [27] measuring the dark signal. The gain coefficient is determined in laboratory measuring the sensor's response of a radiance standard that is illuminated by a known artificial light source [31]. The result of the radiometric correction is a separate hyperspectral data cube for VNIR and SWIR including at-sensor-radiance values.

3.2 Geometrical co-alignment method

The geometric alignment and geocoding procedure consists of four main modules (Fig. 5): a generic photogrammetry processor, a ray tracing module, an automatic, robust-tie point matching algorithm and a cost-function minimizer.

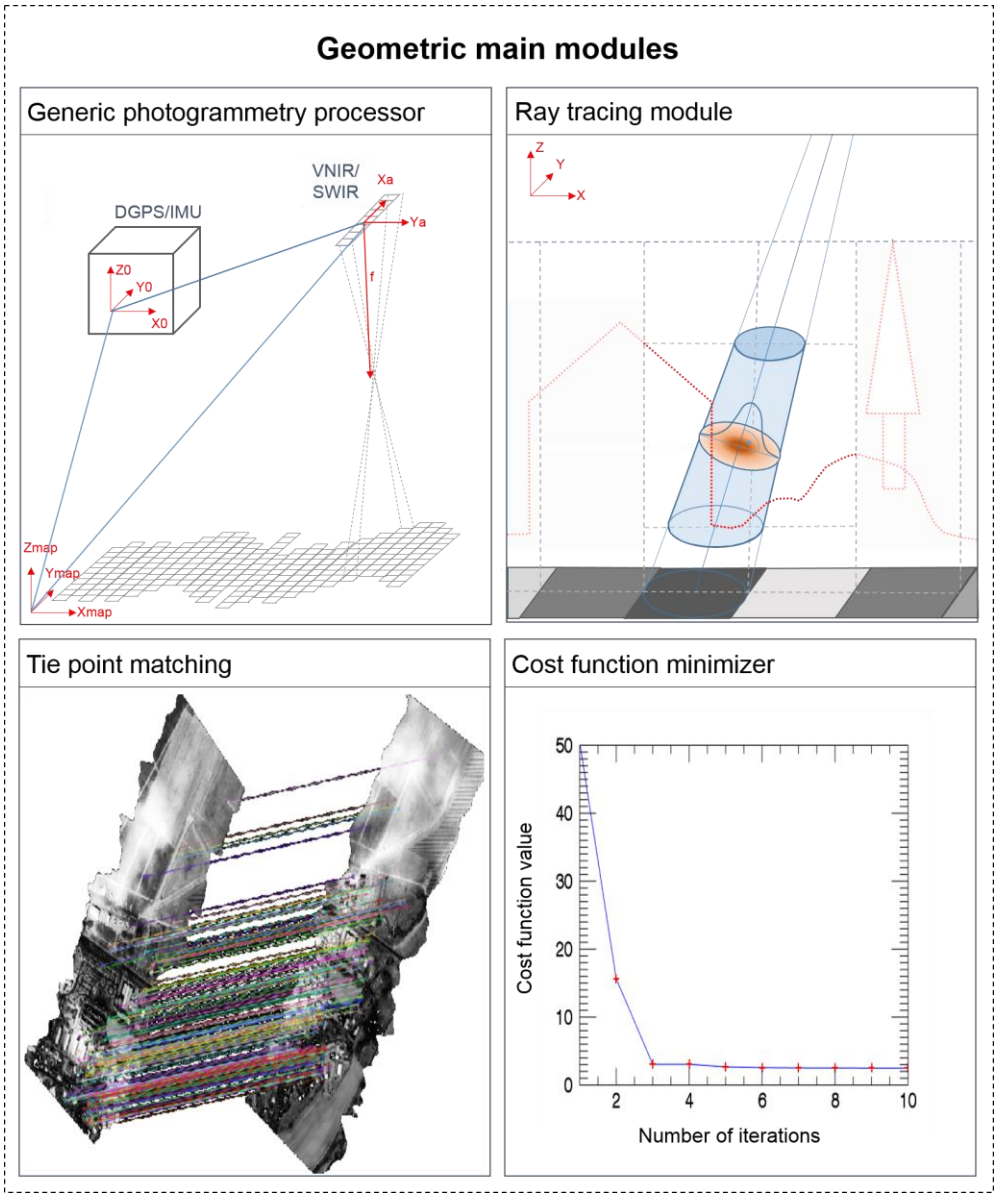

Fig. 5: The four main geometric modules, which are used across the developed geometric alignment procedure.

The central component of the geometric workflow is a generic photogrammetric processor that transforms the image coordinates (Xa, Ya) into map coordinates (Xmap, Ymap). This module is closely linked to a ray tracing module that calculates the elevation (Zmap) on the lidar point cloud. The direct rigorous parametric geocoding is performed based on the generated trajectories, focal length and principle point following the principles of the collinearity equation that define the transformation between the pushbroom scan line image space and the object space. Based on the collinearity equation, the object coordinates of every HSI sensor

element at the minimum elevation (Zmap) projection plane is calculated. The position and attitude for every exposed sensor row is tapped on demand from the original navigation file in its full temporal resolution with sub-row precision. A rigid assignment of a fixed position and attitude with discretization to integral sensor rows is avoided during the alignment and georeferencing process. This ensures synchronization optimization between sensor and DGPS/IMU as well as subpixel matching opportunity based on the original navigation data.

The ray tracing module defines the geometric intersection (Xmap, Ymap, Zmap) of the HSI pointing with the lidar point cloud. In addition, the ray tracing module calculates the lidar points inside a projected cone and their distance to the cone centre. The cones represent the pointing of a HSI pixel. The ray tracing module is always performed subsequent to the photogrammetry processor and with the same procedure. The minimum and maximum elevation projection planes define 3D-line vectors representing the HSI pointing. These 3D-line vectors are shortened iteratively to minimize the potentially neighbouring lidar points. For elevation determination the intersection between this 3D vector line and a TIN (triangulated irregular network) generated from the 3D lidar point cloud is calculated. This is based on a fast triangle line intersection test using barycentric coordinates. The lidar points inside a cone and their distance to the cone centre are calculated by defining the cone with the across and along track instantaneous field of view (IFOV) of the respective sensor pixel. The lidar points inside each cone representing the respective HSI pixel line of sights are indexed and stored in a look up table (LUT). Overall, the space partitioning procedure inside the ray tracing module that handles the point cloud is realized by a 3D histogram based voxel filter.

An automated tie point determination and matching algorithm is required at several processing steps. The developed tie point detection and matching algorithm is based on an established robust feature detector called SIFT (scale invariant feature detection) developed by Lowe [32]. The key point detector is based on finding local maxima in Differences-of-Gaussians (DoG) between adjacent scales. The SIFT key point descriptor vectors are based on gradient histograms of the detected feature points. SIFT tie points are assumed to be scale, rotation and transformation invariant [32]. The applied feature matching is based on minimum Euclidean distance of the descriptor vectors. The feature matching is adapted to the specific sensor characteristics of both sensors concerning masking, maximum spatial match radius and location. The detected tie points are filtered based on the perspective transformation model between the two involved images with RANSAC [33]. Thus, false matches can be robustly removed.

For the parametric co-registration of the HSI data to the lidar data a cost function minimization is essential to improve various extrinsic and intrinsic parameters (Table II) to enhance the average accuracy. Two different cost minimization strategies are involved. A tie-point based and an area-based approach. The area-based is explained in 3.2.2.30. For the tie-point based version approach, the parameters of the collinearity equations are iteratively modified by bisecting the offset parameter intervals. This is realized by varying the involved parameters of the hyperspectral sensor for every single tie point pair. For every iteration the pointing directions are calculated parallel for the respective parameter intervals by the photogrammetry processor. The intersections with the lidar point cloud are calculated by the ray tracing module. The parameter offset which generates the smallest 3D root-mean-square error (RMSE) between the corresponding tie points in object space is the final

offset parameter. The respective starting parameter range and interval size are predefined by the sensor system and integration.

3.2.1 Adjustment of the sensor concerning spectral and spatial responses

One of the essential steps for the fusion of the two sensors is the adaptation and homogenization of the different spectral and spatial sensor responses in order to make them comparable [34] [35]. Due to different spectral and spatial resolutions, the HSI wavelength and bandwidth is adapted to the lidar specification whereas the irregular lidar point intensities are adapted spatially to the HSI response.

The spectral response adaption (Fig. 2 rhomb 5) usually comprise a spectral up-sampling of the HSI using interpolation [36] and a convolution with the assumed SRF of the lidar data [21]. Due to the fact that the spectral bandwidth of one lidar pulse is extremely short, the FWHM of the lidar SRF was expected to be close to zero. Thus the corresponding HSI intensity with the 1550 nm centre wavelength of the lidar was directly interpolated with Hermite Spline. A convolution with the expected SRF of the lidar was not performed.

For the spatial response adaptation the lidar intensity information is adapted spatially to the HSI intensities (1550 nm) (Fig. 2 rhomb 4). Two different methods are applied in the co-registration approach. The normal raster based convolution is described below. In addition to this technique, a dynamic ray tracing based spatial response adaptation is also realized (see 3.2.2.30). The spatial impulse response of an imaging sensor to a point source can be expressed by the point spread function (PSF). The PSF is defined by, among other parameters, the sensor´s electronic, detector, optic, and motion characteristics. The lidar intensity data is resampled from the irregular point information to the prospective grid resolution of the geocoded HSI data (1.5 m). Beyond the resolution, the PSF of the hyperspectral sensor is

considered by convolving the lidar intensities with an approximated PSF using a Gaussian 2D-Function of the HSI sensor. This normal raster based convolution is realized as a first guess and makes the lidar intensity raster spatially comparable to the hyperspectral data. Whereas, the ray tracing approach (see 3.2.2.30) is realized for the final refinement. Both spatial response adaptations depend on sufficiently high lidar point density.

3.2.2 Parametric geometric co-alignment

The parametric geometric co-alignment (Fig. 2 rhomb 6) is based on three processing steps. Fig. 6 represents the detailed workflow of this parametric geometric co-alignment.

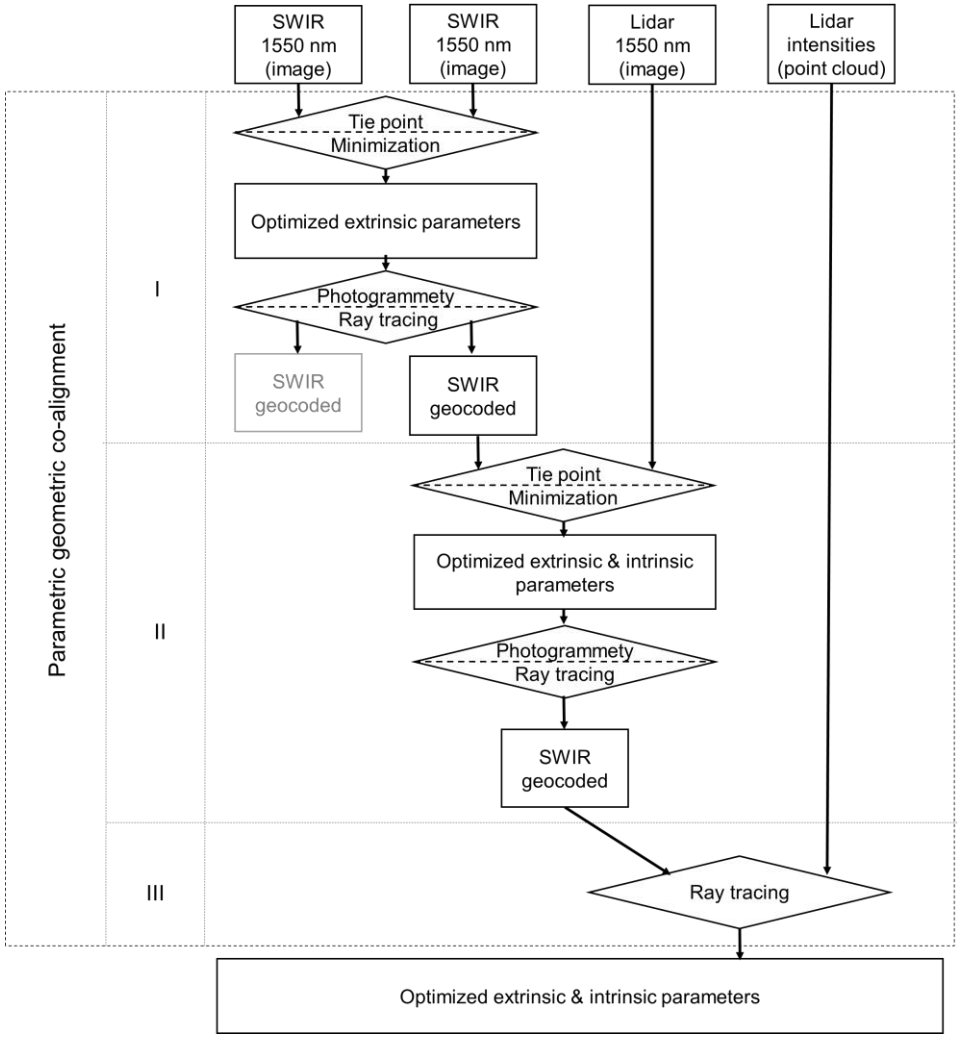

Fig. 6: Detailed workflow of the parametric geometric co-alignment procedure divided in 3 main processing steps; rectangles represent data products; rhombs indicate the applied main processing modules (Fig. 5)

In the first step a boresight calibration of Hyperspectral images is realized. Therefore, robust tie points are generated between the overlapping areas of preliminary geocoded HSI flight stripes (band 1550 nm) using the described tie point matching algorithm. These tie points are utilized inside the cost function minimizer realizing a first approximation of the SWIR sensor boresight. The photogrammetry processor in combination with the ray tracing module assigns the respective coordinates by calculating the intersections between the pointing of the sensor element and the lidar point cloud for the intervals. The boresight variation causing the smallest RMSE between the tie points determines the boresight angle offsets. All HSI SWIR images

are geocoded again using the corrected attitude angles and lidar elevation information.

The second step is the tie-point based parametric co-registration. For every geocoded hyperspectral flight stripe we generate an intensity image (1550 nm) of the overlapping lidar point cloud (see 3.2.1.23.2.1). Tie points are generated automatically based on both overlapping intensity grids. The parametric co-registration procedure is also based on the cost function minimizing module. Subsequently, the refinement of the boresight parameter, a camera resectioning is performed with the same minimizing approach. The camera resectioning encompasses the focal length (f) and the principal point (X0a, Y0a) of the SWIR Hyspex sensor. All in all, eight parameters (roll, pitch, heading, X0a, Y0a, f, synchronization timing Δt, altitude) are adjusted with the cost function minimization module to optimize the accuracy of the co-alignment. gives an overview of the considered parameters and in which co-alignment step they are optimized (symbolized by the crosses).

Table II: Overview of parameters optimized in the co-alignment approach

Parameter type	**Parameter name**	**Abbreviation**	**Co-alignment step**		
			1	**2**	**3**
Extrinsic parameters	Roll		x	x	x
	Pitch		x	x	x
	Heading		x	x	x
	Altitude	Z0		x	x
	Synchronisation timing	Δt		x	
Intrinsic parameters	Principal point	X0a, Y0a		x	x
	Focal length	f		x	x

At most, three variables are optimized together. Correlated variables are optimized separately. The colours in the table indicate the grouping of parameters optimized together. The complete co-registration procedure can be repeated iteratively if necessary.

The fine ray tracing based co-alignment of HSI lines and Lidar intensity data is realized in a third step. The final optimization is realized with an area-based approach by back projecting the lidar intensities to the geometric uncorrected HSI intensities. The minimization of the RMSE between a few tie points for different parameters is not a simple linear description of the planar alignment of the HSI with the lidar reference. An area-based cost aggregation method was developed to refine the offset parameter determination (Fig. 7).

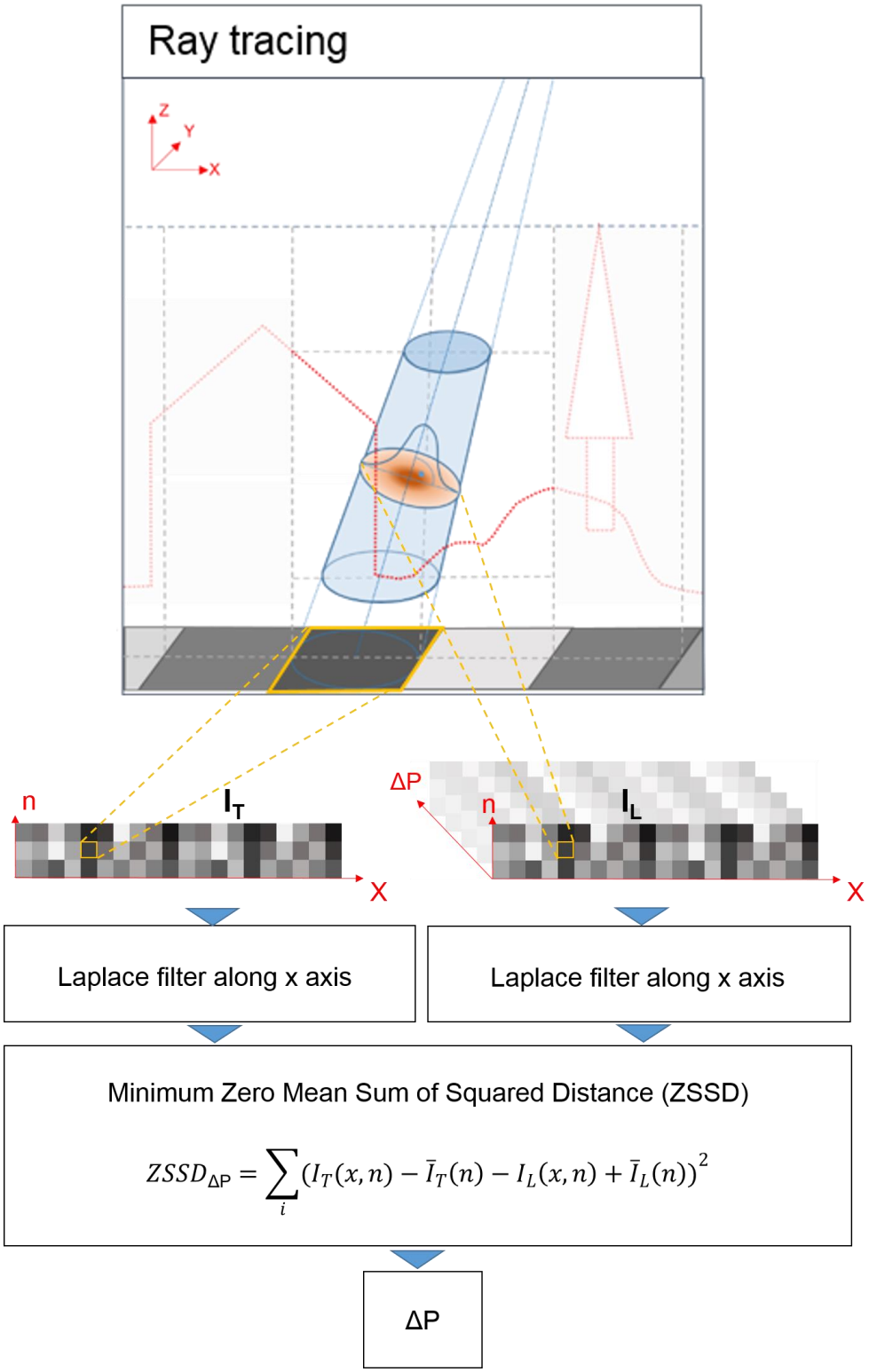

Fig. 7: Ray tracing based refinement of the co-alignment; I_T (Intensity template) = three HSI intensity image rows (x = across track direction, n = along track direction); I_L (Intensity lidar) = corresponding lidar intensities are generated by ray tracing based back projection for different offset parameters (ΔP); the ZSSD is calculated between all Laplacian filtered I_L images and the I_t image for every offset parameters variations (ΔP).

For every pixel of a geometric uncorrected HSI image line (x, n) the corresponding lidar intensity points were collected with the standard ray tracing module. Thus, *the lidar points inside the cone representing the pointing of the corresponding HSI pixel* and their distance to the cone centre is calculated. This is done iteratively for small parameter variations (ΔP) for every HSI pixel using the latest optimized parameters from the previous step and for three selected adjacent image lines (n) that are less effected by shadowing. All intensity values of the collected points inside a pixel beam were weighted with Gaussian PSF centred along the centre axes of the respective HSI cone. Therefore, the spatial response function is correctly approximated in terms of the spatial footprint projection and orientation of the HSI spatial pointing to the surface. For every parameter iteration step a convolution with a Laplace kernel is calculated in across track direction (x) for the respective three adjacent HSI and corresponding lidar intensities. The three lines of the geometrically uncorrected HSI image serve as template (I_T). The generated corresponding lidar intensities (I_L) for varying parameters (Table II) are compared with the HSI template by calculating the Zero Mean Sum of Squared Distance (ZSSD). The offset parameter combination, which generates the match with the smallest ZSSD, is applied globally to refine the geometric correction.

3.3 Geometric correction

Provided that the sensor integration and the sensor model is stable during the flight campaign, the determined offset parameters are valid for all acquired flight strips. Thus, the final procedure is the global assignment of the determined offset parameters to the trajectories and their corresponding SWIR flight stripes. The offset parameters are used inside the photogrammetric processor and the ray tracing module (see 3.2) for all flight stripes. Although the co-alignment of the VNIR sensor

to the SWIR sensor can be realized with the same introduced co-alignment workflow. The spectral and spatial adaptation methods represented in 3.2.1 with the respective sensor parameters and the same parametric co-registration procedure as represented in 3.2.2 can be used. However, as a co-registration reference the already co-registered and spectrally overlapping SWIR band of ~ 979 nm can be used.

4 Results and Discussion

The introduced geometric co-alignment procedure is applied to the data of the conducted calibration flight campaign. It results in a co-registered orthorectified HSI image cube (SWIR), the determined intrinsic sensor parameter, positioning and attitude offsets and an IGM file containing the georeferencing information and height information for each HSI image pixel. In addition, a lidar point lookup table is generated, which allocates all lidar points falling into a HSI pointing.

For our test flight, the accuracy assessment of the co-alignment is realized by a geometric comparison of the co-aligned HSI SWIR intensity image with the lidar intensity image. In addition a short comparison to other related methods is given.

4.1 Comparison of HSI and LIDAR intensities

The first accuracy assessment is based on a manually measured set of 73 regularly distributed tie points (Fig. 8). They result in an RMSE of 0.499 m in XY direction (RMSE of 0.224 m in X and RMSE of 0.446 m in Y direction). Both intensity images have a grid size of 1.5 m per pixel that leads to an RMSE of less than 1/3 of the grid size. Fig. 9 shows the Euclidian distances between related tie points and the histogram of these distances. 85 % local planar offsets are smaller than the RMSE. Only a few points (15 %) have larger offsets that are up to 1.5 m. This indicates a

high accuracy and precision of the global alignment between lidar intensity image and HSI intensity image.

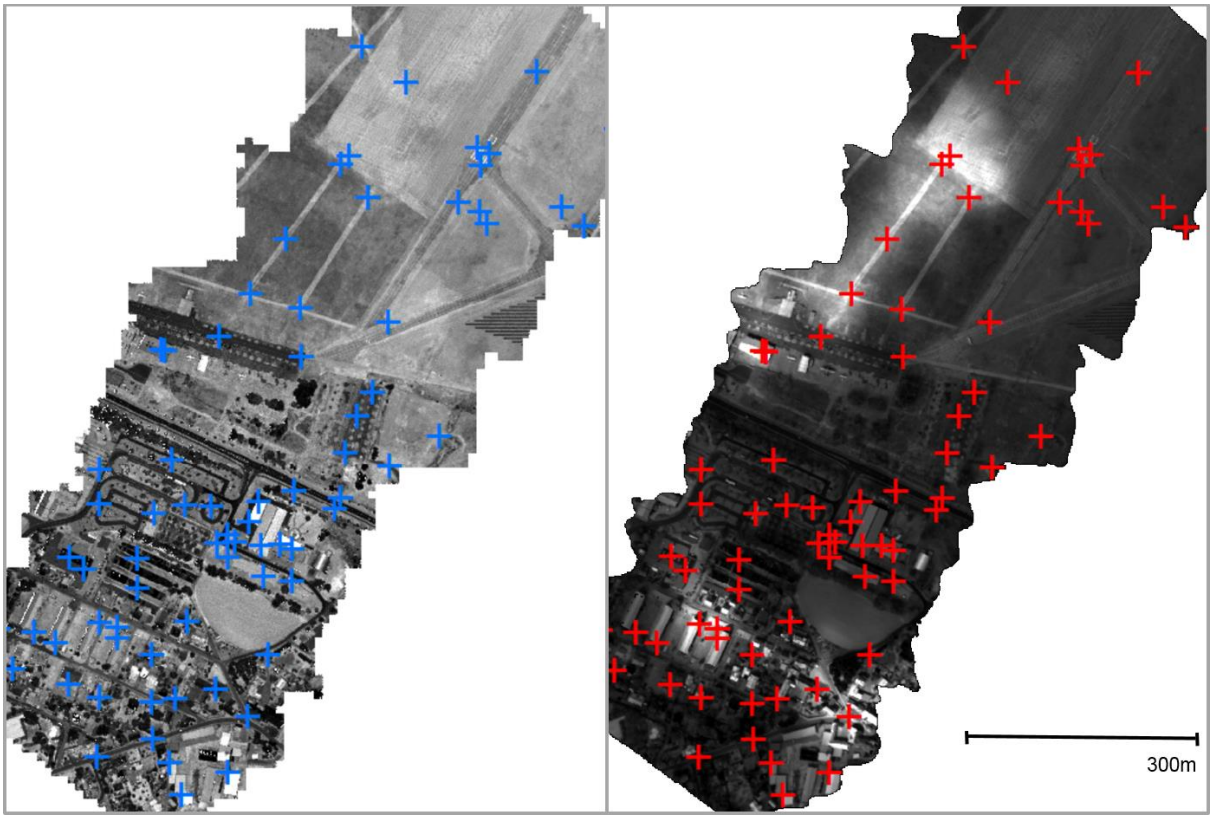

Fig. 8: Accuracy assessment based on 73 manual created tie points; lidar intensity image (left), HSI intensity image (right).

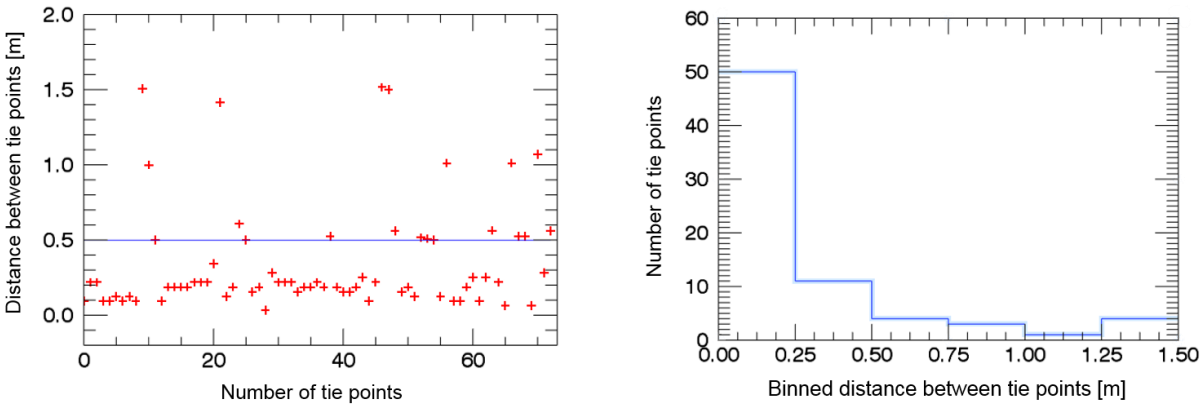

Fig. 9: Euclidian distances between related tie points; blue plot represents the RMSE (left), distance histogram (right)

Tie-point based accuracy assessment gives only limited information about co-alignment accuracy of complex object structures. A visual feature assessment allows for a better local evaluation basis. The indication of how accurate certain structures in

HSI fit to the lidar intensity structures is very important for the overall fusion process. The accuracy of the geometric feature fit is essential for extended classifications of surface objects, especially in spatial and spectral heterogeneous areas. Therefore, a second accuracy assessment was performed, where perceptible linear structures along roads or around building structures were delineated in both intensity images. Fig. 10 gives an overview of the delineated structures, which indicates the global fit of the orthorectified HSI to the lidar intensity. Most of the delineated features exactly overlay along their entire extent. Influences of the stronger perspective distortions towards off-nadir across track are not perceptible. This influences are distinctive for a field of view of about 27.2° and a flight altitude of about 800 m above ground.

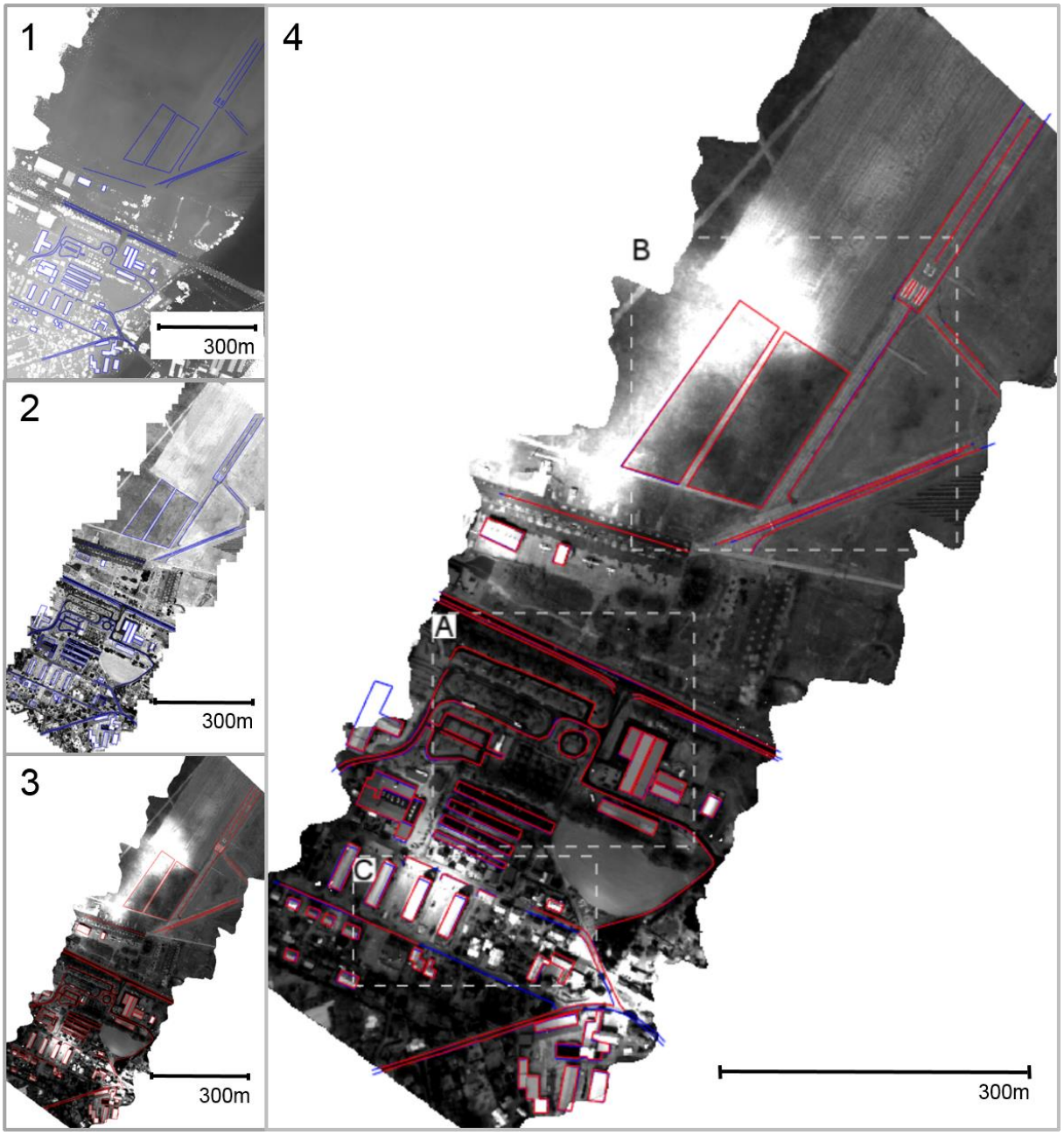

Fig. 10: Overview of accuracy assessment based on delineated structures for subjective evaluation; Structures (blue lines) delineated from a 1-m DSM (1) and lidar intensities (1550 nm) (2), Structures (red lines) delineated from orthorectified SWIR (1550 nm) HSI intensities images (3), Overlay of delineated structures representing the accuracy of geometric description of surface objects (4); In places where only blue lines (lidar intensity features) without corresponding red lines (HSI intensity features) are visible, the delineation was not possible due to shadowing effects.

A detailed visual assessment (Fig. 11) and mathematical assessment (Fig. 12) confirms and refines the result of the overview. Most of the object structures are represented geometrically accurate with subpixel accuracy. Along the structures of the flat terrain of the flight field (Fig. 11 B) and the roads the delineations match

perfectly. In addition, the building structures shown in Fig. 11 A and C are aligned very accurately. Only the buildings in parallel have a clearly perceptible foreshortening of 1-2 pixels in along-track direction, which could not be assigned to the determined offset parameters (Fig. 11 C). This effect can be caused e.g. by nonlinearities in the synchronization timing or position and attitude accuracies. Fig. 12 shows diagrams of the shortest Euclidian distance between the delineated lidar structures and 215,885 points generated along the delineated SWIR structures. The histogram (left) show that more than 95% of the points have a Euclidian distance towards the delineated lidar structures that are smaller than 0.6 pixel. The direction dependency is evaluated with the wind rose diagram (right). Overall, the direction dependency is closely bundled to the main orientation of the delineated structures. Most of the structures are orientated along the axis north-northeast south-southwest and west-northwest east-southeast. These orientations are clearly represented inside the wind rose. However, about 28 % offsets are in north-northeast direction and only about 15 % offsets are in south-southwest direction. This north-northeast trend of accumulation as well as the tendency of larger offset distances in this direction can be attributed to some extend to the shadowing of the objects in the HSI intensities. But the same trend is also visible for the second main axis in west-northwest direction. This cannot be attributed to shadowing effects and gives an indication for still remaining, but very small systematic errors inside the parametric co-alignment procedure. However, the delineation accuracy assessment and their diagrams suggest that most of the significant systematic errors inside the co-alignment procedure are successfully minimized.

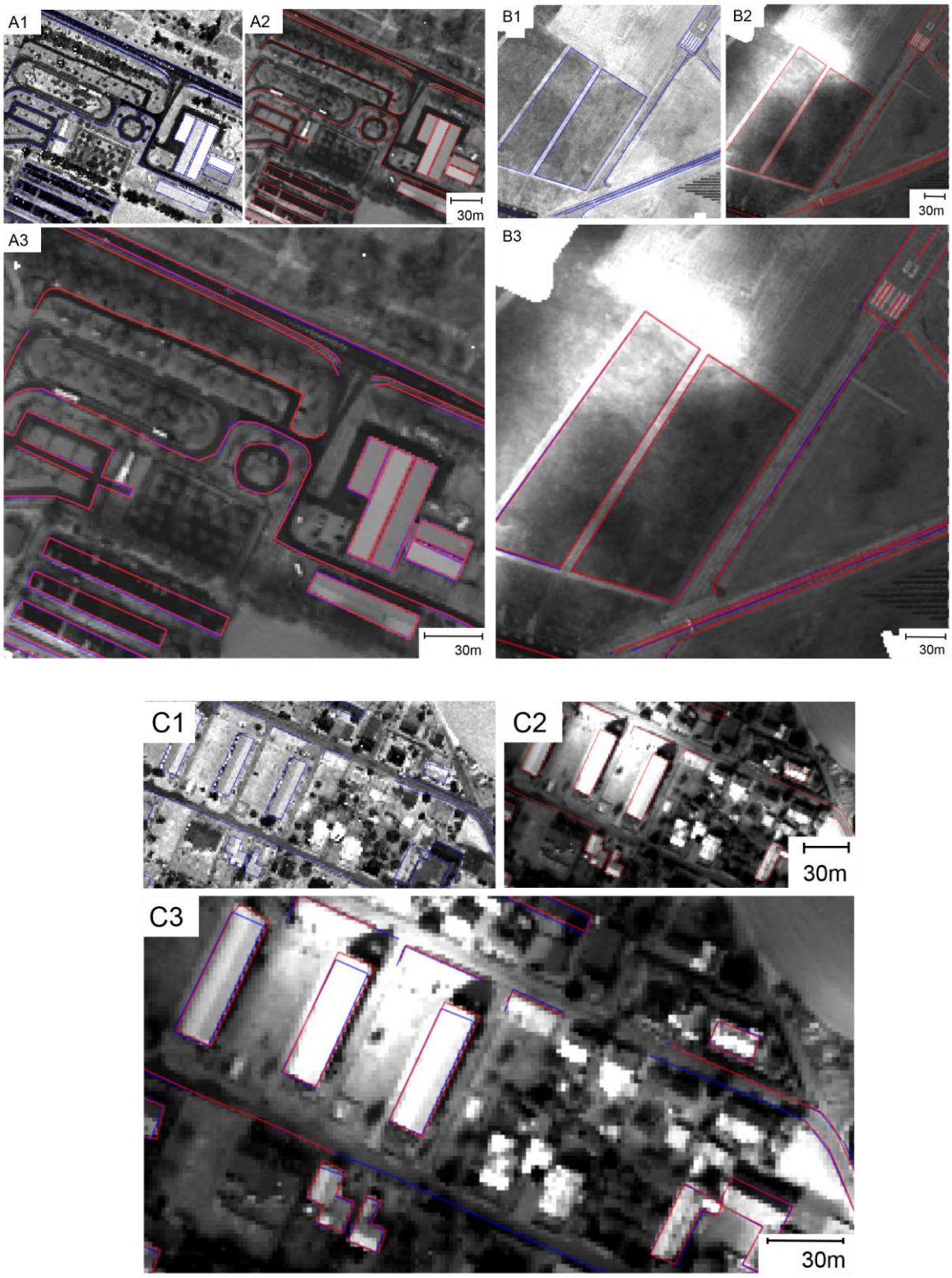

Fig. 11: Detailed assessment of delineated surface structures for 3 (A, B, C) different areas (see Figure 9 for location); blue delineated structures based on lidar intensities (1550 nm) (1), red delineated structures based on SWIR HSI intensities (1550 nm) (2), overlaid delineated structures (3).

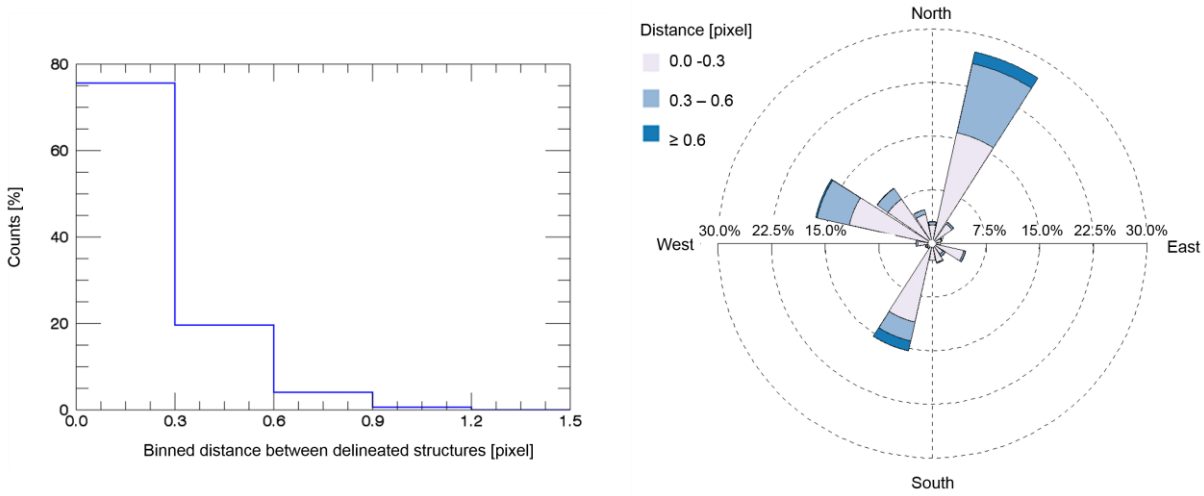

Fig. 12: Histogram of the Euclidian distances between structures delineated from SWIR intensities (red lines in Fig. 10) and structures from lidar intensities (blue lines in Fig. 10) (left). Direction dependency of these Euclidian distances represented by a wind rose diagram (right)

Feature-based methods as well as intensity-based methods strongly rely on the image quality. Especially non-parametric methods need homogeneous distributed image features and homogenous illumination all over the image. The shadowing effects in the HSI images and the different spatial responses of both sensors have been the major challenges for a proper co-registration. The represented co-registration algorithm has proven to have the potential to overcome both problems through carefully chosen parameters. Thus, the determined offset parameters (Table II) are applicable for a complete data acquisition campaign. Despite the clearly perceptible non-optimal illumination conditions due to object and cloud shadowing (Fig. 10), an accurate automatically co-registration was performed. The shadows were problematic during the visual accuracy assessment and it was difficult to visually differentiate between object boundaries and object shadows. The normalized difference image (Fig. 13) gives an overview of the illumination differences between lidar and HSI. The absolute normalized difference image shows more heterogeneous patterns especially in the urban area, which are introduced by the reflection

properties and the exposer of different surface features. But also the variation of laser penetration rates into vegetation lead to significant differences [37]. However, image gradients around objects which would be introduced by geometric misregistrations are not perceptible inside the normalized difference images. All spatial patterns introduced by intensity differences can be attributed to illumination and reflectance issues of the surface objects. The difference images should only give an idea of the diverse intensity responses and how they can be attributed. The differences should not be over interpreted due to the fact that the lidar intensities are not radiometrically calibrated.

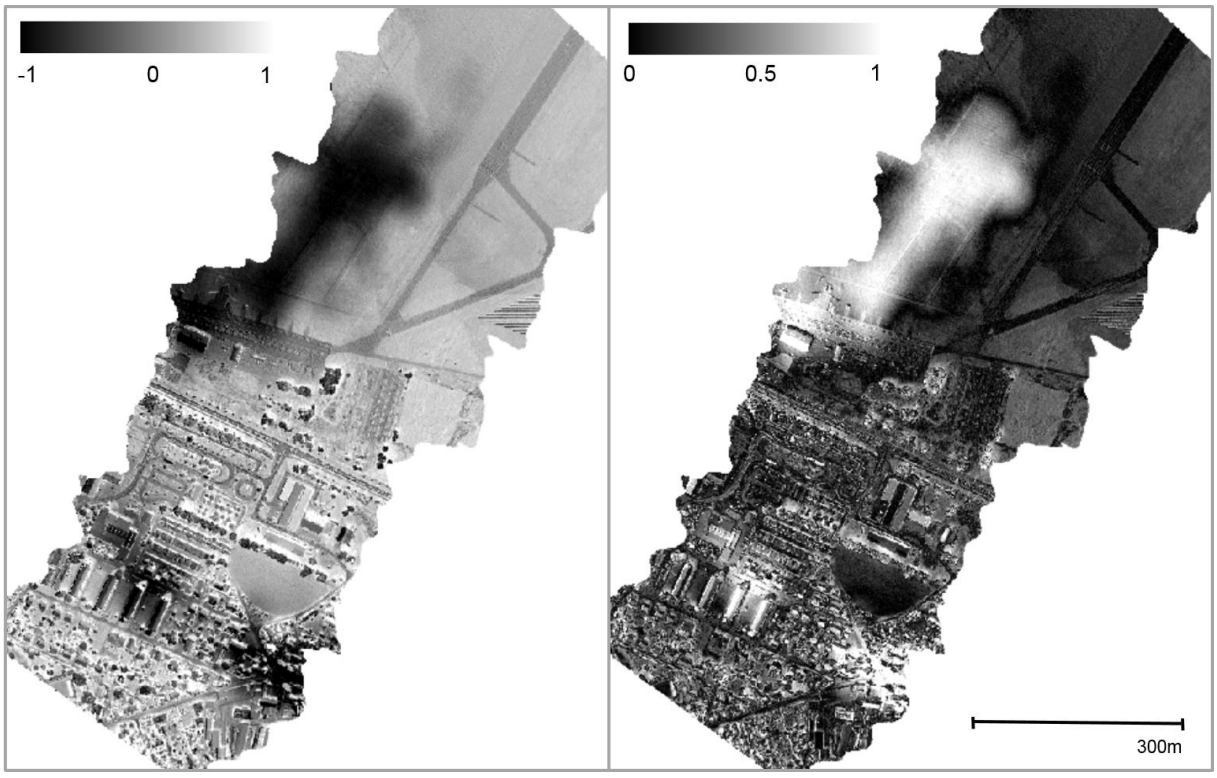

Fig. 13: Normalized difference image (left) and absolute normalized difference image (right) between lidar intensities and HSI intensities. Both intensity images were normalized to values between 0 and 1 by their respective maximum intensities. The normalized HSI intensities were subtracted from the normalized lidar intensities. In the normalized difference image (left), grey areas represent less difference between lidar and HSI. White areas represent the illumination differences introduced by shadowing objects. Black areas represent cloud gaps introducing high intensities in the HSI images. In the absolute normalized difference image (right) black areas represent intensity differences close to zero.

The workflow results from the challenging differences of the spatial and spectral responses. It is not possible to generate enough robust tie points between the adopted lidar intensity image and the HSI image data, before the first coarse geometric co-alignment of the HSI overlapping flight stripes. Only the coarse geometric co-alignment of the HSI overlapping flight stripes and the spectral and spatial adaptation allows for the automatic tie point matching between HSI and lidar intensities. For this purpose, 214 robust tie points were detected between the overlapping SWIR HSI flight lines (3.2.2.1). The boresight determination starts at an RMSE of 50m (boresight offsets propagate in different directions due to apposed flight lines) and results after nine iterations in an RMSE of 2.497 m (Fig. 14 left) between the overlapping SWIR HSI flight lines. A boresight offset of -1.638° for roll, 0.618° for pitch and 0.290° for heading was detected. Additional iterations did not improve the RMSE.

For the parametric co-registration of the HSI image to the lidar intensity image 41 tie points were generated. At the beginning, a misregistration with an RMSE of 3.198 m between HSI and lidar image was measured. The optimization of roll, pitch, heading leads to a RMSE of 1.938 m (Fig. 14 middle). The additional optimization of focal length, principal point, synchronization timing and altitude leads to an improvement of the RMSE to 1.161 m (Fig. 14 right).

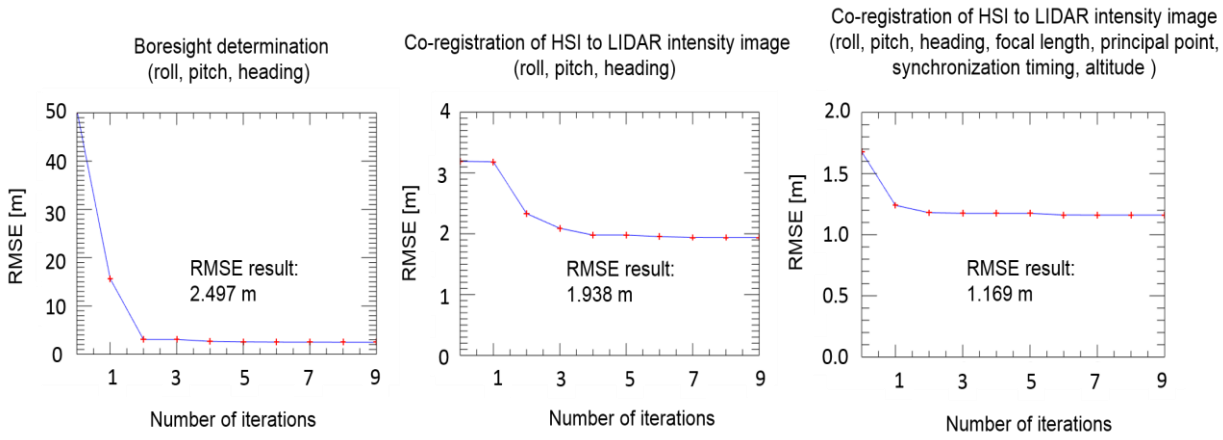

Fig. 14: RMSE optimization using the sequenced geometric alignment procedures.

An iteration of the complete tie-point based parametric co-registration (3.2.2.2) did not lead to perceptible alignment improvements. However, the ray tracing based cost aggregation of complete sensor lines (3.2.2.3) leads to improvement in alignment accuracy. The global accuracy and precision is improved, but especially the local object structure alignment gains form the area-based refinement. The stability of the algorithm is influenced to some extend by the different shading characteristics that are inherent between both images and by the point density of the lidar. Therefore, lines with less shadowing influence should be chosen for the refinement of the co-registration. The final back projection based on ray tracing results in parameter offsets of -1.817° for roll, 0.461° for pitch, 0.231° for heading, 0.251 m for the altitude, 0.033 s for synchronization time (Δt), -0.680 pixel for the focal length (f) and for the principle point -0.607 (X0a) and 0.178 (Y0a).

The adaptation of the overlapping spatial and spectral domains is a requirement for the comparison of both sensors entities with subpixel accuracy. Sufficient tie points can be generated between HSI and lidar intensity images also for off-nadir areas influenced by stronger perspective distortions. The combination of the robust feature detector SIFT, the sensor specific feature matching and the final perspective transformation model (homography) based outlier removal (RANSAC) results in a

very robust tie point detection and matching algorithm. The used minimization procedure is based on computational costly and slow forward projection and bisectioning. But the results appear to be very robust for the parameter minimization incorporating the ray tracing based height determination. Improving the rate of convergence by using gradient minimization techniques appeared less robust than minimizing the pure cost function value based on bisectioning.

For achieving subpixel accuracy, it is necessary to accomplish all processing steps on the original temporal resolution of the pre-processed navigation file. A discretization into integral rows, especially during the parametric minimization procedures, results in a RMSE of only 2/3 of the grid resolution (instead of 1/3 of the grid resolution). The rigorous parametric geocoding procedure incorporates the geometric and spectral sensor model. However, it proves to be very effective to optimize the HSI intrinsic sensor additional to the exterior parameter. Therefore, geometric sensor variations can be compensated in relation to the determined sensor model.

4.2 Comparison to related methods

For a comparison to related methods, the HSI data was also co-registered to the lidar intensity image by using the common HSI direct geocoding software PARGE^{TM} [11]. Therefore a parameter optimization of roll, pitch, heading and altitude was realized based on 27 manually generated and iteratively filtered tie points. This procedure only leads to an RMSE of 3.03 m (about 2 pixel) measured based on 22 independent manually set tie points. This can be only understood as a rough and partially comparison but it indicates the efficiency of the comprehensive proposed method and that a common tie point based boresight alignment does not eliminate all inherent systematic errors. Additional sensor driven, parametric co-registration methods were

not available within the study. A comparison with a feature-based rubber sheeting method is obviously not a good solution due to its non-parametric character and therefore the associated lack of generalization and repeatability for different surface structures and acquisition conditions. Therefore, the presented results can only be theoretically discussed and compared with published and adequate co-alignment techniques. Asner et al. [1] introduced the most comparable approach. With their parametric co-alignment that is completely tie point based they achieve accuracies of "<< 1 pixel RMSE". However, they described the geometric alignment in a more general manner. Despite the lack of the presented ray tracing based back projection and a missing accuracy assessment based on delineated features, the theoretical comparison indicates that the achieved results are appropriate. In addition, the acquisition conditions, sensor design, sensor calibration and sensor integrations differ between the different studies so it is very difficult to make a theoretical and reliable comparison. We emphasize that most published papers focus only on the accuracy assessment of retrieved information from the combination of both data entities and not on the geometric co-alignment. Therefore, this is the first study explicitly focusing on the methodology of intensity based in-flight parametric co-registration between these two sensors types.

This research indicates that one co-alignment approach for its own is not sufficient for an accurate co-alignment between the heterogenic sensors. The stepwise accuracy improvement realized by the introduced 3 step alignment approach shows the evidence of using complementary fundamental and advanced co-registration strategies as well as sensor driven spatial response adaptation techniques beyond standard tie point based approaches also inside parametric approaches. The presented parametric co-alignment approach has the advantage over non-parametric methods that locally derived parameters could be assigned to the global flight

campaign independent from local illumination conditions and detectable surface structures. Additionally, the optimization of 8 extrinsic as well as intrinsic parameters makes the method robust against changes of the sensor model. The approach of parametric compensation of systematic alignment errors between the sensors and its consequent generic sensor driven design, guarantees that the method is highly repeatable and generalizable. The point-feature based algorithm is suitable to match hyperspectral pushbroom sensors and lidar intensity data with subpixel precision. Nevertheless, the alignment accuracy improvements caused by the area-based refinement indicate that the point based approach did not completely characterize the co-alignment. The hybrid co-alignment strategy (point-feature based RMSE and area-based cost aggregation) overcomes the drawbacks of the respective methods. Overall, the ray tracing approach based on lidar point data enables highest accuracy concerning elevation integration and spatial intensity adaptation. It establishes the development of further geometric co-alignment refinement procedures on a vector base. Both approaches in combination allow for co-alignment possibilities without discretization and thus minimize radiometrically relevant resampling errors.

5 Summary

In this study, we presented a parametric, physical based geometric co-alignment of hyperspectral imaging to lidar intensity data. It is shown that the lidar data help to improve the accuracy and precision of georeferenced hyperspectral data in addition to adding elevation information.

The presented hybrid co-alignment methods is based on three processing steps: In a first step, a coarse boresight alignment between overlapping hyperspectral flight stripes is realized. Second, a tie-point based parametric co-alignment of hyperspectral to lidar intensities is performed. The optimization includes extrinsic as

well as intrinsic hyperspectral sensor parameters. The third step is a parametric co-alignment refinement utilizing an area-based cost aggregation between overlapping hyperspectral to lidar intensities. The combination of diverging alignment procedures is necessary because of different sensor responses. It is shown that a ray tracing based back projection of the lidar point intensities and their spatial response adaptation to the geometric uncorrected HSI intensities ensures a subpixel accuracy which is superior to a conventional tie point based approaches. A tie-point based co-alignment by itself is not sufficient to describe the overall geometric accuracy of the alignment. The area-based cost aggregation however is able to compensate these lacks and increases the geometric alignment accuracy. Altogether, it is advisable to optimize the intrinsic parameters of the HSI sensors additionally to the extrinsic offset parameters to reduce the entire error budget of the co-alignment. The lidar point intensity as well as the elevation information has the potential to stabilize the geometric pre-processing workflow at least for relatively flat but heterogeneous terrain. The fusion of both data entities results in geometrically co-aligned data, achieving accuracies of 1/3 pixel with high precision.

Our results indicate that the hybrid utilization of tie-point based and area-based cost aggregation appears to be very promising. The approach provides the basis for a comprehensive physical fusion of hyperspectral and lidar data.

Acknowledgements

The authors would like to thank the Helmholtz Centre Potsdam - GFZ German Research Centre for Geosciences and the funding program “Zentrales Innovationsprogramm Mittelstand (ZIM)” founded by the Federal Ministry for Economic Affairs and Energy Germany (BMWi) for financial support. Special thanks

for instrumental and technical support concerning the complete lidar part and flight campaign goes to MILAN Geoservice GmbH namely Dirk Hannusch.

References

[1] G. P. Asner, D. E. Knapp, J. Boardman, R. O. Green, T. Kennedy-Bowdoin, M. Eastwood, R. E. Martin, C. Anderson, und C. B. Field, „Carnegie Airborne Observatory-2: Increasing science data dimensionality via high-fidelity multi-sensor fusion“, *Remote Sensing of Environment*, Bd. 124, S. 454–465, Sep. 2012.

[2] U. Heiden, W. Heldens, S. Roessner, K. Segl, T. Esch, und A. Mueller, „Urban structure type characterization using hyperspectral remote sensing and height information“, *Landscape and Urban Planning*, Bd. 105, Nr. 4, S. 361–375, Apr. 2012.

[3] A. Brook, E. Ben-Dor, und R. Richter, „Fusion of hyperspectral images and LiDAR data for civil engineering structure monitoring“, in *2010 2nd Workshop on Hyperspectral Image and Signal Processing: Evolution in Remote Sensing (WHISPERS)*, 2010, S. 1–5.

[4] H. Buddenbaum, S. Seeling, und J. Hill, „Fusion of full-waveform lidar and imaging spectroscopy remote sensing data for the characterization of forest stands“, *International Journal of Remote Sensing*, Bd. 34, Nr. 13, S. 4511–4524, 2013.

[5] T. U. Kampe, B. R. Johnson, M. A. Kuester, und M. Keller, „NEON: the first continental-scale ecological observatory with airborne remote sensing of vegetation canopy biochemistry and structure“, *J. Appl. Remote Sens Journal of Applied Remote Sensing*, Bd. 4, Nr. 1, S. 043510, 2010.

[6] B. Koetz, G. Sun, F. Morsdorf, K. J. Ranson, M. Kneubühler, K. Itten, und B. Allgöwer, „Fusion of imaging spectrometer and LIDAR data over combined radiative transfer models for forest canopy characterization“, *Remote Sensing of Environment*, Bd. 106, Nr. 4, S. 449–459, Feb. 2007.

[7] M. Dalponte, L. Bruzzone, und D. Gianelle, „Fusion of Hyperspectral and LIDAR Remote Sensing Data for Classification of Complex Forest Areas“, *IEEE Transactions on Geoscience and Remote Sensing*, Bd. 46, Nr. 5, S. 1416–1427, 2008.

[8] M. Alonzo, B. Bookhagen, und D. A. Roberts, „Urban tree species mapping using hyperspectral and lidar data fusion“, *Remote Sensing of Environment*, Bd. 148, S. 70–83, Mai 2014.

[9] B. Cook, L. Corp, R. Nelson, E. Middleton, D. Morton, J. McCorkel, J. Masek, K. Ranson, V. Ly, und P. Montesano, „NASA Goddard's LiDAR, Hyperspectral and Thermal (G-LiHT) Airborne Imager“, *Remote Sensing*, Bd. 5, Nr. 8, S. 4045–4066, Aug. 2013.

[10] G. P. Asner, D. E. Knapp, T. Kennedy-Bowdoin, M. O. Jones, R. E. Martin, J. Boardman, und C. B. Field, „Carnegie airborne observatory: in-flight fusion of hyperspectral imaging and waveform light detection and ranging for three-dimensional studies of ecosystems“, *Journal of Applied Remote Sensing*, Bd. 1, Nr. 1, S. 013536–013536, 2007.

[11] D. Schläpfer und R. Richter, „Geo-atmospheric processing of airborne imaging spectrometry data. Part 1: Parametric orthorectification“, *International Journal of Remote Sensing*, Bd. 23, Nr. 13, S. 2609–2630, 2002.

[12] E. P. Baltsavias, „A comparison between photogrammetry and laser scanning“, *ISPRS Journal of photogrammetry and Remote Sensing*, Bd. 54, Nr. 2, S. 83–94, 1999.
[13] R. Muller, M. Lehner, R. Muller, P. Reinartz, M. Schroeder, und B. Vollmer, „A program for direct georeferencing of airborne and spaceborne line scanner images“, *International Archives of Photogrammetry Remote Sensing and Spatial Information Sciences*, Bd. 34, Nr. 1, S. 148–153, 2002.
[14] R. Richter und D. Schläpfer, „Geo-atmospheric processing of airborne imaging spectrometry data. Part 2: atmospheric/topographic correction“, *International Journal of Remote Sensing*, Bd. 23, Nr. 13, S. 2631–2649, 2002.
[15] H. Torabzadeh, F. Morsdorf, und M. E. Schaepman, „Fusion of imaging spectroscopy and airborne laser scanning data for characterization of forest ecosystems – A review“, *ISPRS Journal of Photogrammetry and Remote Sensing*, Bd. 97, S. 25–35, Nov. 2014.
[16] J. Avbelj, D. Iwaszczuk, R. Müller, P. Reinartz, und U. Stilla, „Coregistration refinement of hyperspectral images and DSM: An object-based approach using spectral information“, *ISPRS Journal of Photogrammetry and Remote Sensing*, Bd. 100, S. 23–34, Feb. 2015.
[17] J. Lee, X. Cai, C.-B. Schonlieb, und D. A. Coomes, „Nonparametric Image Registration of Airborne LiDAR, Hyperspectral and Photographic Imagery of Wooded Landscapes“, *IEEE Transactions on Geoscience and Remote Sensing*, Bd. 53, Nr. 11, S. 6073–6084, Nov. 2015.
[18] D. Schlapfer, J. Nieke, und K. I. Itten, „Spatial PSF Nonuniformity Effects in Airborne Pushbroom Imaging Spectrometry Data“, *IEEE Transactions on Geoscience and Remote Sensing*, Bd. 45, Nr. 2, S. 458–468, Feb. 2007.
[19] M. T. Eismann, *Hyperspectral remote sensing*. Bellingham, WA: SPIE, 2012.
[20] R. A. Schowengerdt, *Remote Sensing: Models and Methods for Image Processing*. Academic Press, 2006.
[21] L. Guanter, K. Segl, B. Sang, L. Alonso, H. Kaufmann, und J. Moreno, „Scene-based spectral calibration assessment of high spectral resolution imaging spectrometers“, *Optics Express*, Bd. 17, Nr. 14, S. 11594, Juli 2009.
[22] C. Rogass, M. Brell, K. Segl, T. Kuester, und H. Kaufmann, „Automatic reduction of keystoneapplications to EnMAP“, in *Proceedings of the 8th EARSeL SIG imaging spectroscopy workshop; EARSeL*, 2013.
[23] A. Wehr und U. Lohr, „Airborne laser scanningan introduction and overview“, *ISPRS Journal of Photogrammetry and Remote Sensing ISPRS Journal of Photogrammetry and Remote Sensing*, Bd. 54, Nr. 2–3, S. 68–82, 1999.
[24] E. P. Baltsavias, „Airborne laser scanning : basic relations and formulas“, *ISPRS journal of photogrammetry & remote sensing. Amsterdam.* -, Bd. 54, S. 2–3, 1999.
[25] P. Gege, J. Fries, P. Haschberger, P. Schötz, H. Schwarzer, P. Strobl, B. Suhr, G. Ulbrich, und W. Jan Vreeling, „Calibration facility for airborne imaging spectrometers“, *ISPRS Journal of Photogrammetry and Remote Sensing*, Bd. 64, Nr. 4, S. 387–397, Juli 2009.
[26] A. Baumgartner, P. Gege, C. Köhler, K. Lenhard, und T. Schwarzmaier, „Characterisation methods for the hyperspectral sensor HySpex at DLR's calibration home base“, in *SPIE Remote Sensing*, 2012, S. 85331H–85331H.
[27] K. Lenhard, A. Baumgartner, und T. Schwarzmaier, „Independent Laboratory Characterization of NEO HySpex Imaging Spectrometers VNIR-1600 and SWIR-320m-e“, *IEEE Transactions on Geoscience and Remote Sensing*, Bd. 53, Nr. 4, S. 1828–1841, Apr. 2015.

[28] L. Guanter, K. Segl, und H. Kaufmann, „Simulation of Optical Remote-Sensing Scenes With Application to the EnMAP Hyperspectral Mission“, *IEEE Transactions on Geoscience and Remote Sensing*, Bd. 47, Nr. 7, S. 2340–2351, Juli 2009.
[29] „HySpex, Norsk Elektro Optikk“. [Online]. Verfügbar unter: http://www.hyspex.no/index.php. [Zugegriffen: 19-Mai-2015].
[30] „RIEGL - RIEGL Laser Measurement Systems“. [Online]. Verfügbar unter: http://www.riegl.com/. [Zugegriffen: 19-Mai-2015].
[31] C. Rogass, C. Mielke, D. Scheffler, N. Boesche, A. Lausch, C. Lubitz, M. Brell, D. Spengler, A. Eisele, K. Segl, und L. Guanter, „Reduction of Uncorrelated Striping Noise—Applications for Hyperspectral Pushbroom Acquisitions“, *Remote Sensing*, Bd. 6, Nr. 11, S. 11082–11106, Nov. 2014.
[32] D. G. Lowe, „Distinctive image features from scale-invariant keypoints“, *International journal of computer vision*, Bd. 60, Nr. 2, S. 91–110, 2004.
[33] M. A. Fischler und R. C. Bolles, „Random Sample Consensus: A Paradigm for Model Fitting with Applications to Image Analysis and Automated Cartography“, *Commun. ACM*, Bd. 24, Nr. 6, S. 381–395, Juni 1981.
[34] K. Segl, L. Guanter, C. Rogass, T. Kuester, S. Roessner, H. Kaufmann, B. Sang, V. Mogulsky, und S. Hofer, „EeteS - The EnMAP End-to-End Simulation Tool“, *IEEE Journal of Selected Topics in Applied Earth Observations and Remote Sensing*, Bd. 5, Nr. 2, S. 522–530, Apr. 2012.
[35] D. Schläpfer, A. Boerner, und M. Schaepman, „The potential of spectral resampling techniques for the simulation of APEX imagery based on AVIRIS data“, in *Summaries of the Eighth JPL Airborne Earth Science Workshop, JPL, Pasadena (CA)*, 1999, Bd. 99, S. 377–384.
[36] C. Rogass, K. Segl, C. Mielke, Y. Fuchs, und H. Kaufmann, „Engeomap—a Geological Mapping Tool Applied to the Enmap Mission“, *EARSeL eProceedings*, Bd. 12, S. 94–100, 2014.
[37] M. Alonzo, B. Bookhagen, J. P. McFadden, A. Sun, und D. A. Roberts, „Mapping urban forest leaf area index with airborne lidar using penetration metrics and allometry“, *Remote Sensing of Environment*, Bd. 162, S. 141–153, Juni 2015.